Using silicon disk resonators to measure mechanical losses caused by an electric field

Cite as: Rev. Sci. Instrum. 93, 014501 (2022); doi: 10.1063/5.0076311 Submitted: 23 October 2021 • Accepted: 13 December 2021 • **Published Online: 4 January 2022**







Y. Yu. Klochkov, L. G. Prokhorov, M. S. Matiushechkina, R. X. Adhikari, Dand V. P. Mitrofanov Dela



AFFILIATIONS

- ¹ Faculty of Physics, Lomonosov Moscow State University, 119991 Moscow, Russia
- ²Institute for Gravitational Wave Astronomy, University of Birmingham, Birmingham B15 2TT, United Kingdom
- ³Laser Interferometry and Gravitational Wave Astronomy, Max Planck Institute for Gravitational Physics, 30167 Hannover, Germany
- LIGO Laboratory, California Institute of Technology, Pasadena, California 91125, USA

ABSTRACT

Several projects of the next generation gravitational-wave detectors use the high purity monocrystalline silicon test masses. The electric field of the actuator that is applied to correct the position of the silicon test mass causes additional mechanical losses and associated noise. Disk mechanical resonators are widely used to study mechanical losses in multilayer optical coatings that are deposited on the test masses of gravitational-wave detectors. We use silicon disk resonators to study losses caused by an electric field. In particular, the dependence of mechanical losses on the resistivity of silicon is investigated. The resonator is a thin commercial silicon wafer in which a low frequency nodal diameter mode is excited. A DC voltage is applied between the wafer and a nearby electrode. We use two measurement configurations. In the first configuration, the dependence of losses on the resistance in the voltage supply circuit is investigated. The dependence of losses on the resistivity of silicon is investigated in the second configuration. We propose a model that relates the electric field induced mechanical loss in disk resonators to the resistivity of the material. Measurements are carried out for low and high resistivity silicon wafers. The measurement results are compared with calculations. Based on these studies, it is possible to estimate the loss and noise of the test masses of gravitationalwave detectors associated with electrostatic actuators.

Published under an exclusive license by AIP Publishing. https://doi.org/10.1063/5.0076311

I. INTRODUCTION

Several years have passed since the first direct detection of gravitational waves.1 Laser interferometric gravitational-wave (GW) detectors LIGO and Virgo are working successfully.2-Japan's KAGRA detector joined the network of GW observatories.5 Researchers were faced with the challenge of improving the current generation of GW detectors and developing more sensitive next generation detectors. In one of the possible design options for the implementation of the Einstein Telescope and Cosmic Explorer projects of future GW detectors, test masses of detectors and their suspensions will be made of high purity monocrystalline silicon and cooled to low temperatures.

Silicon was chosen for its low internal mechanical losses, suitable thermal properties, and low optical absorption at wavelengths of 1.5-2.5 µm.8 To correct the position of the test masses of the

GW interferometric detectors, electrostatic actuators are used which create an electric field between the test mass and electrodes of the actuator.9 Unlike the dielectric fused silica test masses of the current GW detectors, the application of an electric field to the oscillating semiconductor silicon test mass results in the additional mechanical loss and thermal noise associated with this loss. 10 This loss is caused by electric currents flowing in the oscillating conductive body due to the change in the capacitance between it and the electric field electrode. This mechanism of electrical or Ohmic losses was especially evident in MEMS/NEMS systems, for example, in electromechanical resonators fabricated from graphene, carbon nanotubes, and nanowires due to their very small effective masses and strong charge -13 There is also electrostatic damping that depends on the surface properties of the vibrating body and the electrodes.

Disk mechanical resonators in which nodal diameter modes are excited are widely used to study mechanical losses in multilayer high

a) Author to whom correspondence should be addressed: vpmitrofanov@physics.msu.ru

reflectivity thin film optical coatings deposited on the test masses of current and next generation GW detectors. ^{15–20} We propose to use disk resonators made of high-purity silicon to study mechanical losses caused by an electric field. Note that it is also possible to investigate these losses in silicon disks with optical coatings on their surface.

In this article, we describe an experimental setup developed for studying losses in silicon disk mechanical resonators caused by an electric field. The resonator is a thin commercial silicon wafer in which a low-frequency nodal diameter mode is excited. A DC field is created when an electric voltage is applied between the wafer and nearby electrodes. In order to reduce anchor losses in disk resonators, a nodal support technique was used. 16,21 An even greater reduction in anchor losses was achieved using the so-called Gentle Nodal Suspension (GNS) technique. 22,23

Unfortunately, we could not use the GNS technique for fixing disk resonators since the electric field creates the instability of the equilibrium position of the resonator. For this reason, we clamp the disk between two stems in the center of the disk. In particular, the dependence of mechanical losses on the resistivity of silicon is investigated. We use two measurement configurations. The first measurement configuration, called the two-electrode configuration, allows us to study the dependence of the electric field induced frequency shift and mechanical loss on the parameters of the electric voltage supply circuit. In the second four-electrode measurement configuration, we study the dependence of the frequency shift and loss on the resistivity of silicon. We propose a model that relates the loss measured in the four-electrode configuration to the resistivity of silicon. The measurement results are compared using calculations.

II. EXPERIMENTAL SETUP AND MEASUREMENT PROCEDURE

As resonators, we used commercial (Virginia Semiconductor, Inc.) double side polished silicon wafers with a diameter of 50.8 mm and a thickness of 0.27 mm. The wafer has two flats as shown in Fig. 1(a). The flats with lengths of 16 and 8 mm cut into sides of the wafer indicate the crystallographic plane (100) and the type of silicon. A lot of vibration modes can be excited in the wafer. We chose a bending mode with two nodal diameters so that one of the diameters passed through the middle of the longest length flat. This mode has a natural frequency of about 800 Hz.

The silicon wafer was clamped between two stems mounted in an aluminum frame as shown in Fig. 2. The wafer was grounded through contact with the spherical surface of the upper stem. The bottom stem was mounted in a spring-loaded manner and had a hemispherical PTFE tip. The radius of curvature of the spherical surface was about 20 mm. This value provided a small contact area necessary to reduce frictional clamping losses and sufficient for the convenience of installing a silicon wafer. This issue was discussed in Refs. 21 and 22.

The ring-shaped electrode divided into four sectors was located over the silicon wafer. The electrodes were etched on a fiberglass copper clad plate and gold-plated, as shown in Fig. 1(b). A pattern of electrodes creating an electric field corresponds to the distribution of displacements in the vibration mode. The orientation of the plate with the electrodes was set so that the cuts in the ring electrode coincided with the middle of the flats of the wafer through which

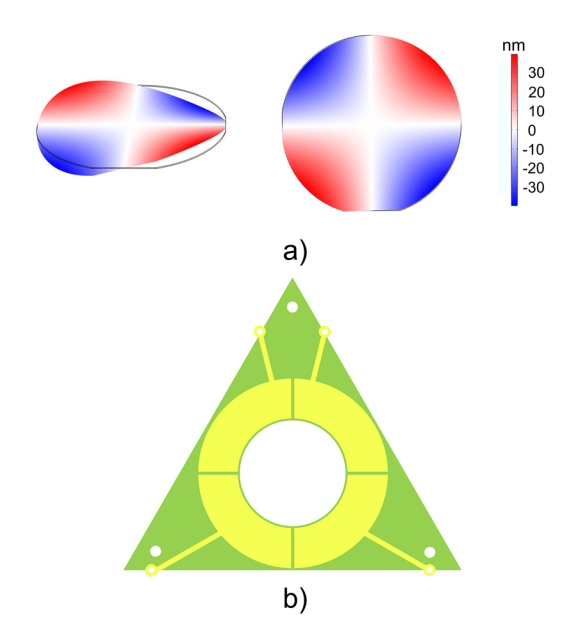


FIG. 1. (a) Vibration mode of the wafer simulated through COMSOL. The color indicates the value of the displacement amplitude in a direction orthogonal to the wafer surface. The typical displacement amplitude used in this work is shown in the color bar. (b) Schematics of the fiberglass copper clad plate with etched and gold-plated electrodes.

the nodal diameter of the selected mode passes. Voltage could be applied separately to every sector. A separation gap of about 0.3 mm between the wafer and the electrode plate was adjusted using three spring-loaded screws, as shown in Fig. 2.

To estimate the gap size, the capacitance meter Mastech MS6013 was connected to the wires attached to the electrodes. The capacitance was measured for the working separation gap and for the 2.4 mm gap set using a calibrated plate. These measurements allowed us to subtract the parasitic capacitance and calculate the capacitance between the wafer and the electrode. The gap size was calculated using the formula for the capacitance of a flat capacitor. The measurement uncertainty of the gap size was about 0.02 mm.

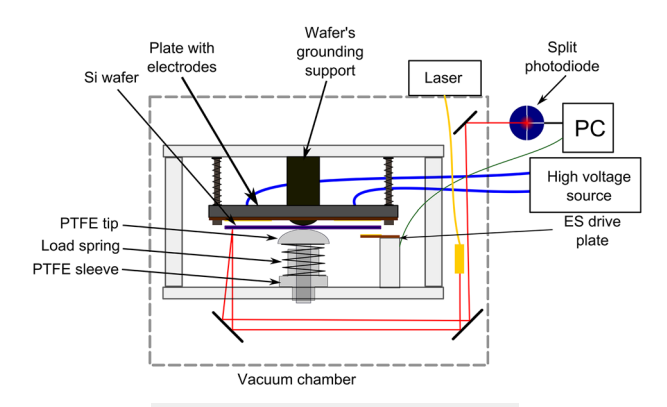


FIG. 2. Schematic of the experimental setup.

The wafer vibration was excited resonantly with the AC voltage (up to 300 V) at a half of the mode resonant frequency using a capacitive electrostatic drive, the plate of which was located under the wafer of about 1 mm below its surface. The dependence of the force between the capacitor plates on the square of the applied voltage leads to the appearance of the doubled frequency of the applied AC voltage in the force spectrum. The wafer vibration was monitored using the optical sensor. The laser beam hits the surface of the sample at the point spaced 3-5 mm from the edge near the nodal diameter of the investigated mode where the local tilt of the surface is maximal during vibration. The local tilt of the wafer produced by its vibration results in a deflection of the laser beam reflected from the wafer surface. The reflected beam passes through a system of mirrors and is detected by a split quadrant photodiode (QPD) placed outside the vacuum chamber. Custom-developed software based on LabVIEW was used to obtain the mode frequency f and the decay time τ from the photodiode signal measured during the wafer free vibration decay. The frame with the clamped wafer was placed in a vacuum chamber with a residual gas pressure of about 10⁻⁵ Torr. The residual gas damping gave a negligible contribution to the measured mechanical loss.

A circuit for applying the DC voltage U_0 to electrodes is shown in Fig. 3. The resistor R_{ex} is a variable external resistor (we can neglect the contribution of the small internal resistance of the voltage source). We used this resistor in order to study a mechanism of the loss caused by an electric field. C_s is a parasitic capacitance that does not change with the wafer vibration. The contribution to it mainly comes from the capacitance between the wires connecting the electrodes to the voltage source and surrounding grounded conductors. R_c is the electrical contact resistance between the silicon wafer and the metal stem. Through it, the wafer is connected to a terminal of the DC voltage source and is grounded. Grounding prevents the accumulation of static electric charges on the wafer, which can be a source of additional non-controlled mechanical losses. 25 The contact resistance R_c depends on the contact materials, state of the contacting surfaces, the clamping force, and other factors.

We used two measurement configurations. In the first configuration called the two-electrode configuration, one pair of electrodes, for example, "1" (see Fig. 3), was connected to the DC voltage source.

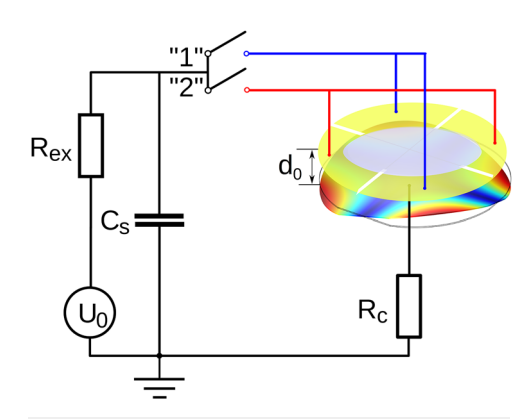


FIG. 3. Circuit for applying the DC voltage U_0 to electrodes.

Another pair of electrodes was grounded. In this case, when the silicon wafer vibrates, the capacitances between each of the two sectors and the wafer change in phase. These changes add up and induce a current in the external circuit. Operation in the two-electrode configuration allows us to study the loss mechanism associated with the relaxation process of the change in the electric charge on the wafer. The vibration of the wafer leads to the change in the capacitance between the wafer and the electrodes, which results in the change in the electric charge and the electric current flowing through the resistance in the voltage supply circuit (including the external resistor R_{ex} , the contact resistance R_{c} , and the wafer resistance R_{w}). This leads to the loss of the vibration energy. The relaxation time can be changed by changing the value of the external resistor R_{ex} .

In the second measurement configuration called the four-electrode configuration, the DC voltage U_0 was applied to all four electrodes and the change in the total capacitance between the silicon wafer and electrodes caused by the wafer vibration was close to zero due to antiphase vibrations in the adjacent quarter sectors of the wafer. Hence, with the full compensation, there is no current in the external circuit and therefore no associated loss. The loss in the four-electrode configuration is caused by the redistribution of the induced electric charge in the wafer and the corresponding electric current flowing through it. This loss depends on the wafer resistivity.

The mechanical loss Q^{-1} is calculated from the decay time τ of the vibration mode with the resonant frequency f according to the relation $Q^{-1}=(\pi f\tau)^{-1}$. The electric field induced mechanical loss Q_E^{-1} was determined as a difference between Q_U^{-1} measured when the voltage U_0 was applied to the electrodes and Q_0^{-1} measured when all the electrodes were grounded,

$$Q_E^{-1} = Q_U^{-1} - Q_0^{-1}. (1)$$

III. CALCULATION OF THE ELECTRIC FIELD INDUCED LOSS AND FREQUENCY SHIFT IN THE MECHANICAL OSCILLATOR

To analyze the mechanism of mechanical losses caused by the relaxation process in the DC voltage supply circuit, consider the electromechanical system with lumped parameters shown in Fig. 4. A mass m of the mechanical oscillator with a natural frequency $\omega_0 = \sqrt{(k/m)}$, where k is a stiffness of the spring, performs a periodical motion x(t). The change in the gap $d(t) = d_0 + x(t)$ leads to the change in the capacitance between the mass and the electrode $C(t) = C_0/(1 + x(t)/d_0)$. Using the condition $x(t) \ll d_0$ in the first order approximation in $x(t)/d_0$, we obtain the equations for the total charge q(t) in the total capacitance $C(t) + C_s$ and the equation for the mass displacement x(t), whereas on the right side, there is an expression for the electrostatic force acting between the plates of the capacitor,

$$\dot{q} = \frac{U_0}{R} - q \frac{1 + \beta x/d_0}{RC_1},$$

$$m\ddot{x} + kx = -\frac{\beta^2 q^2 [1 - 2(1 - \beta)x/d_0]}{2C_0 d_0},$$
(2)

where $C_1 = C_0 + C_s$ and $\beta = C_0/C_1$

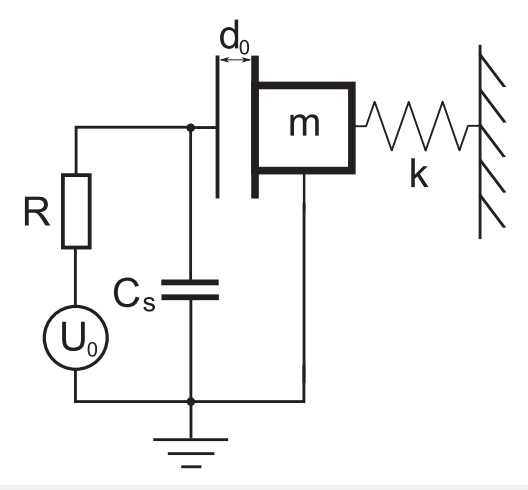


FIG. 4. Model of the electromechanical system used for the calculation of the electric field induced loss and frequency shift in the mechanical oscillator.

An approximate solution to these differential equations is given in the Appendix. It has been found that the electric field introduces the additional negative stiffness k_E and loss Q_E^{-1} into the oscillator. The additional negative stiffness results in the relative change in the oscillator's frequency $(\Delta \omega/\omega_0)_E$,

$$\left(\frac{\Delta\omega}{\omega_0}\right)_E = -\frac{1}{2} \left(\frac{U_0}{d_0}\right)^2 \frac{C_0}{m\omega_0^2} \left[\frac{C_0}{C_1} \frac{1}{1 + (\omega_0 R C_1)^2} + \left(1 - \frac{C_0}{C_1}\right)\right], \quad (3)$$

$$Q_E^{-1} = \left(\frac{U_0}{d_0}\right)^2 \frac{C_0^2}{m\omega_0^2 C_1} \frac{\omega_0 R C_1}{1 + (\omega_0 R C_1)^2}.$$
 (4)

Equation (4) and the first term in square brackets of Eq. (3) describe the loss and the relative change in the resonant frequency, which are typical for the relaxation process with the relaxation time $\tau_{rel} = RC_1$.

The silicon disk mechanical resonator is a system with distributed parameters. We can introduce the effective mass m and the effective capacitance C_0 for the working mode of the wafer vibration in order to use these equations for the analysis of the experimental data. The circuit shown in Fig. 4 does not take into account the resistance of the silicon wafer R_w and the electrical contact resistance R_c between the wafer and the metal stem that is used to clamp the wafer. The contact resistance is difficult to control. The contact resistance and the wafer resistance are not shunted by the parasitic capacitance C_s for the electric current generated due to the wafer vibration. We separated the loss associated with these resistances from the loss associated with the external resistor R_{ex} .

When operating in the four-electrode configuration, the losses of the resonator associated with the resistance in the DC voltage supplying circuit and the contact resistance are significantly reduced. This allows us to investigate the electric field induced loss caused by the silicon resistivity. The silicon wafer vibration leads to the change in the local capacitances between the disk and the electrode. When

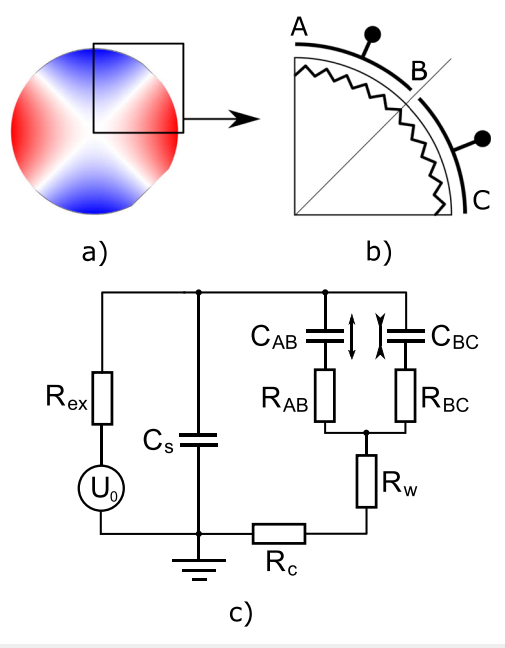


FIG. 5. (a) Distribution of the wafer displacement amplitude in a direction orthogonal to its surface. (b) Model of a distributed RC line used for the calculation of the redistribution of electric charges on the wafer. (c) Equivalent electrical circuit with varying capacitances between the wafer and the electrodes. The distributed capacitances and resistances of the wafer are replaced with equivalent lumped elements C_{AB} , C_{BC} , R_{AB} , and R_{BC} . Arrows near capacitors C_{AB} and C_{BC} show antiphase changes in their capacitances.

the voltage U_0 is applied to the electrode, the vibration causes a redistribution of electric charges in an annular strip of the silicon disk in accordance with the distribution of the vibration amplitude of the wafer [see Fig. 5(a)].

Taking into account the symmetry of the wafer vibrations, the disk can be partitioned into four identical sectors so that each sector is located between the maximum values of the vibration amplitude at points A and C. At the nodal point B, the deflection of the sample changes the sign. In each sector, an annular strip of a silicon disk and an electrode located above it form an electrical resistive–capacitive line, as shown in Fig. 5(b). In the annular strip of each sector, a redistribution of charges occurs, caused by an antiphase change in the capacitance of two distributed capacitors C_{AB}^* and C_{BC}^* with per-unit-length capacitance $c = \varepsilon_0 w/d_0$ and a distributed resistor R_{AC}^* with per-unit-length resistance $r = \rho/wh$, where ε_0 is the vacuum permittivity, ρ is the electrical resistivity of silicon, w is the width of the strip, d_0 is a separation gap between the electrode and the silicon disk, and h is the disk thickness.

If L is a total length of the strip on the disk along which the current flows, then the total resistance of the sector strip is $R_{AC} = R_{AB} + R_{BC} = \rho L/4wh$ and the capacitance of the strip on a half of the sector is $C_{AB} = C_{BC} = \varepsilon_0 Lw/8d_0$. The equivalent electrical circuit with varying capacitances between the wafer and the electrodes is shown in Fig. 5(c). A value of L is defined as the length of a circle drawn in the middle of the annular electrode.

A distributed RC line can be characterized by a number of time-constants. We choose the dominant one as an approximation. It has the maximum value and is expressed through the lumped values of the total capacitance C and resistance $R^{.26}$ $\tau_{RC} \approx (4/\pi^2)RC \approx 0.405 RC$. Taking into account that the capacitances of half-sectors are connected in series between themselves and the strip resistance, we obtain the following for the considered sector:

$$\tau_s \approx \frac{4}{\pi^2} RC/2 = \frac{\varepsilon_0 \rho L^2}{16\pi^2 d_0 h}.$$
 (5)

We assume that the main mechanism of the electric field induced mechanical loss of the silicon disk is the relaxation process associated with the gap capacitance and the disk resistivity. It is described by the equations similar to Eqs. (3) and (4) with the replacement of R_{ex} , C_0 , and C_1 to the corresponding parameters of the wafer and electrodes. The parasitic capacitance C_s for this system is assumed to be negligible. In this case, $\omega_0 \tau_{rel} \ll 1$, and we obtain

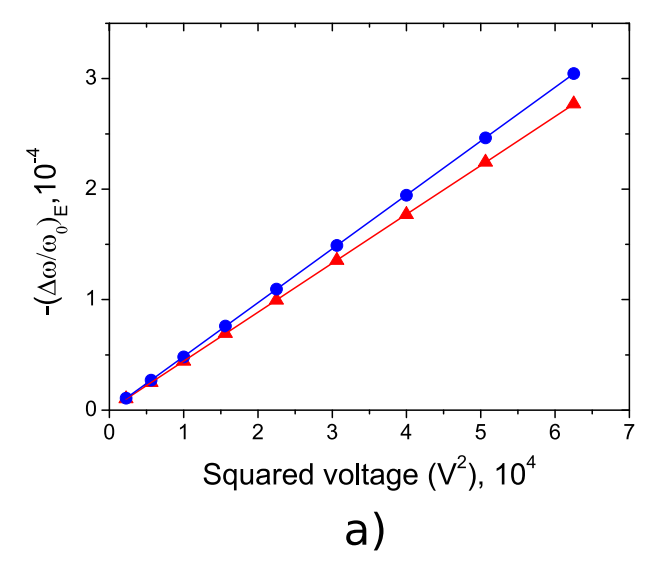
$$Q_E^{-1} = -2\left(\frac{\Delta\omega}{\omega_0}\right)_E \omega_0 \tau_{rel}. \tag{6}$$

Substituting in Eq. (6) the measured value of the relative frequency shift and $\tau_{rel} = \tau_s$, we obtain an estimate of the electric field induced mechanical loss of the disk resonator, caused by the silicon resistivity.

IV. RESULTS OF MEASUREMENTS AND THEIR DISCUSSION

Vibration modes of the silicon wafers were identified from the measured eigenfrequencies by comparing them with the calculated ones using the finite element modeling with COMSOL Multiphysics modeling software. We present the measurement results for two silicon wafers with different resistivities. The low resistivity (LR) wafer No. 1 was fabricated from boron doped silicon with a resistivity of $(1.0 \pm 0.5) \Omega$ cm. It had the resonant frequency of $f_1 \approx 873$ Hz for the working mode with two nodal diameters. The high resistivity (HR) wafer No. 2 was fabricated from undoped silicon with a resistivity of $(1.6 \pm 0.1) \times 10^4 \Omega$ cm. It had the working mode frequency of $f_2 \approx 832$ Hz. In the absence of an electric field, the decay time of the freely decaying vibration amplitude of the silicon resonators was found to be of about 11 s. This corresponds to the mechanical loss $Q_0^{-1} = 3.5 \times 10^{-5}$. One of the main mechanisms of losses is the thermoelastic loss associated with heat flow through the disk as it vibrates. The calculated thermoelastic loss for such a resonator is $Q_{TE}^{-1} \approx 2 \times 10^{-5}$. It can be assumed that the remaining losses were mainly the clamping loss and the surface loss. When an electric voltage was applied to the electrodes, the mode frequency and the decay time were measured in both measurement configurations. The electric field induced mechanical loss Q_E^{-1} was calculated according to Eq. (1).

The electric field induced relative frequency shift and loss measured for both wafers in the two-electrode measurement configuration as a function of a square of the applied voltage are shown in Figs. 6(a) and 6(b). The separation gap of $d_0 = (0.32 \pm 0.02)$ mm was set for the HR wafer and $d_0 = (0.27 \pm 0.02)$ mm for the LR wafer. The experimental data are well approximated by a square function of the voltage in accordance with Eqs. (3) and (4). Notice that the loss measured for the HR wafer is much



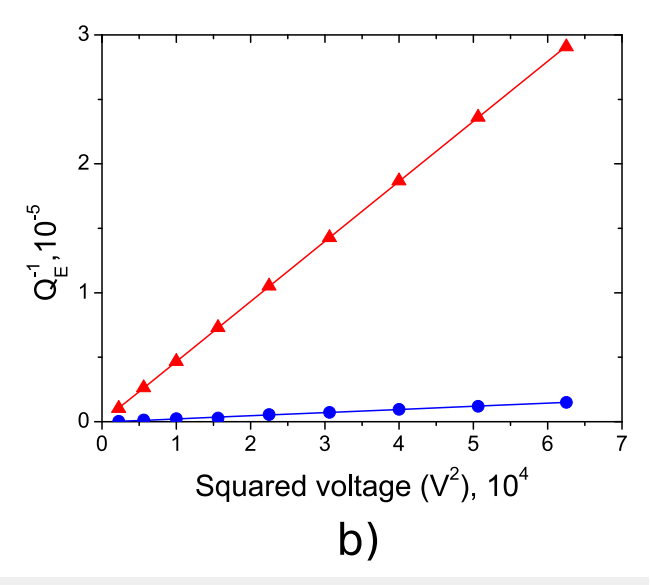
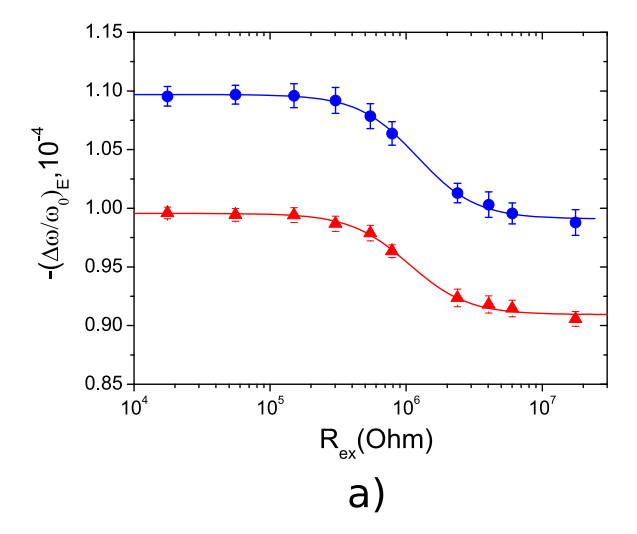


FIG. 6. Electric field induced relative frequency shift $(\Delta w/\omega_0)_E$ (a) and loss Q_E^{-1} (b) of HR (red triangles) and LR (blue circles) silicon wafers measured as a function of a square of the applied voltage U^2 in the two-electrode measurement configuration. Fitted results are shown by solid lines. The separation gap is $d_0=0.32$ mm for the HR wafer and $d_0=0.27$ mm for the LR wafer. The resistor $R_{\rm ex}=17~{\rm k}\Omega$ was included in the voltage supply circuit.

higher than that measured for the LR wafer. We will discuss this in more detail below. The electric field induced relative frequency shift and loss of both wafers measured in the two-electrode measurement configuration as a function of a value of the external resistor R_{ex} included in the voltage supply circuit ($U_0 = 150 \text{ V}$) are shown in Figs. 7(a) and 7(b). The results do not depend on the polarity of the applied voltage within the measurement errors.



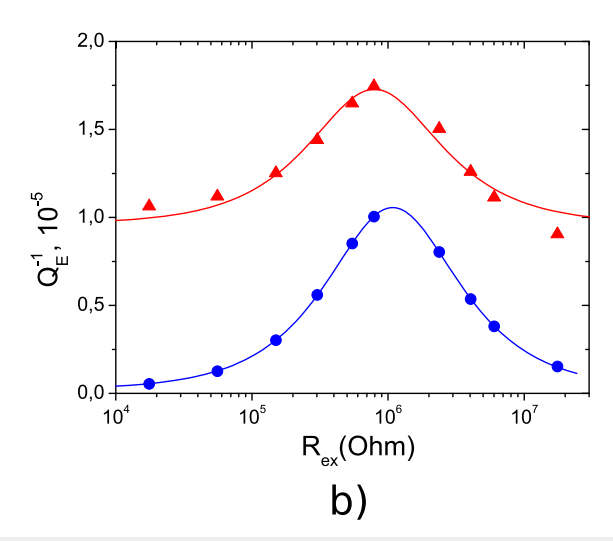


FIG. 7. Electric field induced relative frequency shift (a) and loss (b) of HR (red triangles) and LR (blue circles) silicon wafers measured in the two-electrode measurement configuration as a function of a value of the external resistor $R_{\rm ex}$ in the voltage supply circuit. Fitted results are shown by solid curves. The separation gap is $d_0=0.32$ mm for the HR wafer and $d_0=0.27$ mm for the LR wafer. The applied voltage is U=150 V.

The measured data for the relative frequency shift were fitted with the model Eq. (3) and for the loss with Eq. (4). A constant term that takes into account the loss associated with the contact resistance R_c and the wafer resistance R_w has been added to Eq. (4). Thus, the

fitting formulas look the same although the constant terms in them had different meanings,

$$\left(\frac{\Delta\omega}{\omega_0}\right)_E = A_1 \frac{1}{1 + (B_1 R_{ex})^2} + D_1,\tag{7}$$

$$Q_E^{-1} = A_2 \frac{B_2 R_{ex}}{1 + (B_2 R_{ex})^2} + D_2.$$
 (8)

We used the Origin 8.5 software to calculate fitting parameters. The fitted results are shown by the solid lines in Figs. 6 and 7.

The calculated fitting parameters are presented in Table I. The standard errors of fitting parameters are small although the relationships between parameters $A_1 = -A_2/2$ and $B_1 = B_2$ are found to have large errors. Apparently, this is a consequence of the inaccuracy of the model while taking into account the influence of the contact resistance R_c and the resistance of the wafer R_w . Nevertheless, we can consider that the model satisfactorily describes the experimental data

The four-electrode measurement configuration was used to study the dependence of the electric field induced loss on the silicon wafer resistivity. The electric field induced relative frequency shift and loss of both wafers measured as a function of a square of the applied voltage in the four-electrode measurement configuration are shown in Fig. 8. The experimental data are well approximated by a quadratic dependence on the applied voltage. Only in the case of losses measured for the LR wafer, a large scatter of the experimental data is observed. This is due to small values of the electric field induced losses, which are calculated as the difference between two large values.

The electric field induced frequency shift and loss of the LR and HR silicon wafers measured in the four-electrode measurement configuration as a function of a value of the external resistor R_{ex} in the voltage supply circuit are shown in Fig. 9. In contrast to the two-electrode configuration, the frequency shifts are almost independent of the value of the external resistance R_{ex} for both samples and the loss of the HR wafer. Although for the LR wafer a small peak of losses is still observed, it is about 50 times smaller than the peak observed in the two-electrode measurement configuration and is associated with the incomplete compensation of the local capacitance changes caused by the wafer vibration. For the HR wafer, the peak is not visible due to high background losses, which are obviously caused by its higher resistivity.

Substituting in Eq. (6) the measured relative frequency shift for the HR wafer $(\Delta\omega/\omega_0)_E = (1.8 \pm 0.1) \times 10^{-4}$ and the calculated time-constant $\tau_{rel} = \tau_s$, we obtain an estimate of the electric field induced mechanical loss of the HR silicon wafer, associated with the silicon resistivity. The calculated estimate of Q_E^{-1} was found to be 3×10^{-6} for the applied voltage U = 150 V. The value

TABLE I. Fitting parameters calculated from experimental data.

| Sample | $-A_1, 10^{-5}$ | $B_1(\Omega^{-1}), 10^{-7}$ | $D_1, 10^{-4}$ | $A_2, 10^{-5}$ | $B_2(\Omega^{-1}), 10^{-7}$ | $D_2, 10^{-6}$ |
|----------------|-------------------|-----------------------------|---------------------|---------------------|-----------------------------|----------------------------------|
| LR wafer No. 1 | (1.07 ± 0.02) | (8.6 ± 0.3) | (0.990 ± 0.002) | (2.067 ± 0.007) | (9.24 ± 0.03) | $(0.17 \pm 0.02) (9.6 \pm 0.4)$ |
| HR wafer No. 2 | (0.86 ± 0.02) | (9.6 ± 0.5) | (0.910 ± 0.002) | (1.5 ± 0.2) | (12.5 ± 2.0) | |

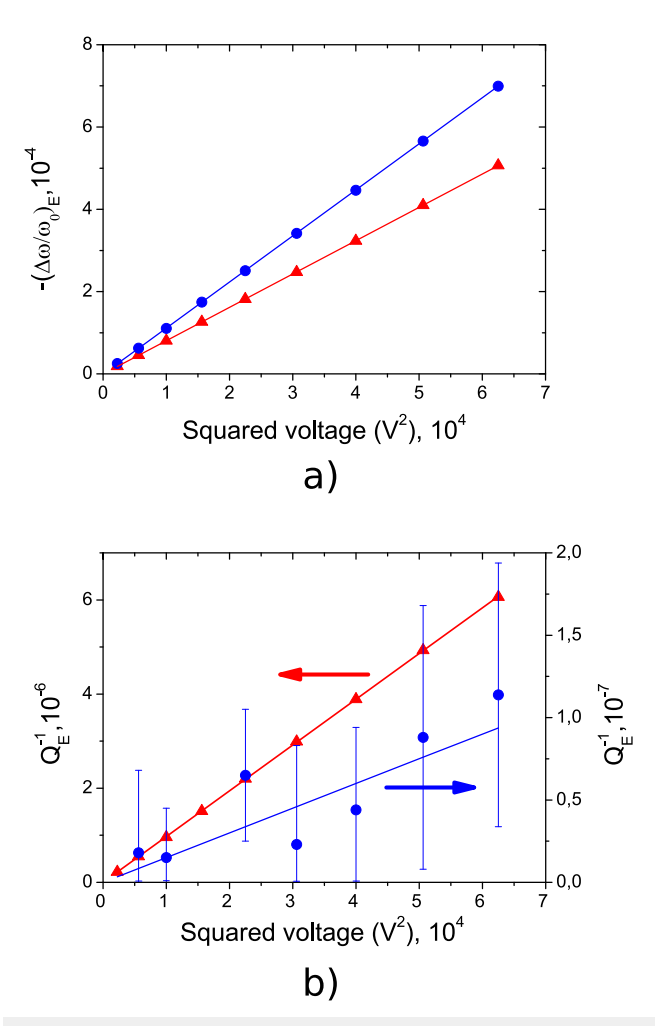
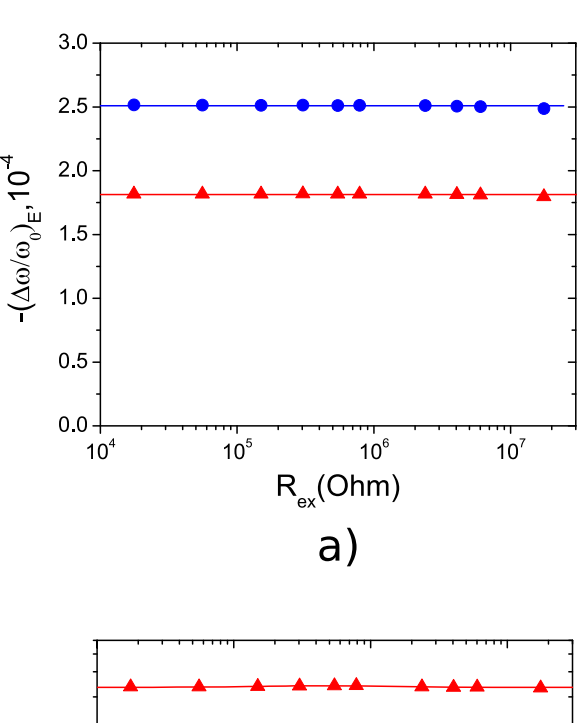


FIG. 8. Electric field induced relative frequency shift $(\Delta\omega/\omega_0)_E$ (a) and loss Q_E^{-1} (b) of the HR silicon wafer (red triangles, left axis) and LR silicon wafer (blue circles, right axis) measured as a function of a square of the applied voltage U^2 in the four-electrode measurement configuration. Fitted results are shown by solid lines. The separation gap is $d_0=0.32$ mm for the HR wafer and $d_0=0.27$ mm for the LR wafer. The resistor $R_{\rm ex}=17~{\rm k}\Omega$ was included in the voltage supply circuit.

 $Q_E^{-1} = (2.3 \pm 0.1) \times 10^{-6}$ was measured for the HR wafer in the four-electrode measurement configuration. This is a satisfactory agreement between the measured and the estimated loss, given the approximate calculation.

For the LR wafer, the calculated estimate of Q_E^{-1} associated with the wafer resistivity was found to be 3×10^{-10} for the applied voltage U = 150 V. The loss value $Q_E^{-1} = (6 \pm 3) \times 10^{-8}$ was measured for the LR wafer in the four-electrode measurement configuration with the resistor $R_{ex} = 17$ k Ω that was small in comparison with the loss peak resistor. In this case, the calculated loss is much less than the uncertainty of the measurement. It is also possible that the losses are associated not with the resistivity of the silicon wafer, but, for example, the properties of its surface 14 contribute to the measured electric field induced losses.



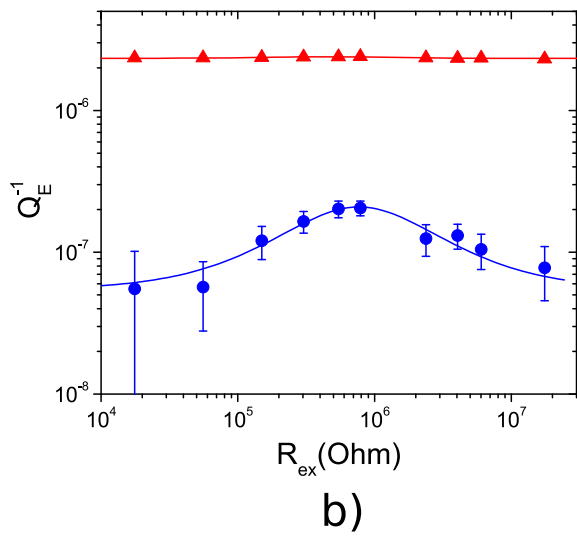


FIG. 9. Electric field induced frequency shift and loss of HR (red triangles) and LR (blue circles) silicon wafers measured in the four-electrode measurement configuration as a function of a value of the external resistor $R_{\rm ex}$ in the voltage supply circuit. Fitted results are shown by solid curves. The separation gap is $d_0=0.32$ mm for the HR wafer and $d_0=0.27$ mm for the LR wafer. The applied voltage is U=150 V.

In order to compare the measured electric field induced losses with the calculated ones using Eq. (6), we made several measurements for each silicon wafer using a new clamping of the wafer each time. Since the size of the gap between the wafer and the plate with electrodes was slightly different each time, the values of the losses were reduced to a single gap of 0.32 mm using the electric field induced frequency shift. For this purpose, the relationship between the gap and the frequency shift obtained from the measurements was

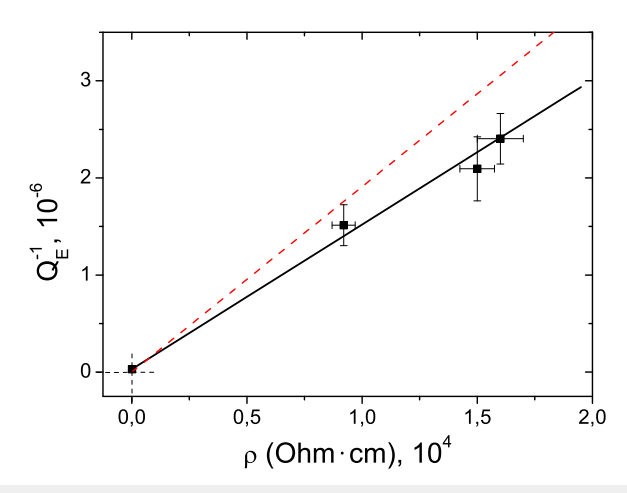


FIG. 10. Electric field induced loss of HR wafers as a function of the silicon resistivity. $R_{\rm ex}=17~{\rm k}\Omega$ and $U=150~{\rm V}$. Loss values obtained for different samples are recalculated to the same separation gap $d_0=0.32~{\rm mm}$ via the frequency shift—the gap relation. Fitted results are shown by the black solid line. Theoretical estimation [according to Eq. (6)] is shown with the red dashed line.

used. Such measurements were also performed for two more silicon wafers with high resistivity. The average values of the electric field induced loss measured for three HR silicon wafers and one LR wafer in the four-electrode measurement configuration as a function of the resistivity are shown in Fig. 10. The experimental data were fitted with a linear function (black solid line). Its slope was found to be $(1.5\pm0.1)\times10^{-10}~(\Omega~cm)^{-1}$. The straight line with a slope of $1.9\times10^{-10}~(\Omega~cm)^{-1}$ (red dashed) corresponds to Eq. (6). Taking into account the approximations made in the modeling, the agreement between the measured loss and the theoretical estimate can be considered satisfactory for the HR silicon wafers.

V. CONCLUSION

We described an experimental setup to measure mechanical losses in silicon disk resonators caused by the electric field applied between the disk and nearby electrodes. Such measurements are important for calculating the losses introduced by electrostatic actuators to the oscillations of the test masses of next generation GW detectors. For the resonators, we used commercial double side polished silicon wafers in which a low-frequency nodal diameter mode was excited. A vibration-induced change in capacitance between the electrode and the silicon resonator leads to a change in the interaction force between them, with a phase lag characteristic of the relaxation process. As a result, the additional negative stiffness and loss were introduced into the resonator. Two different configurations of the electric field were used for measurements. In the two-electrode measurement configuration, we studied the dependence of the electric field induced frequency shift and loss on the external parameters of the DC voltage supply circuit. In the fourelectrode measurement configuration, we studied the dependence of the electric field induced frequency shift and loss on the resistivity of the silicon. A model was proposed to relate electrical losses in the silicon disk resonator to silicon resistivity. Measurement results

for low and high resistivity silicon wafers were presented. A satisfactory agreement between the measured and the estimated loss was obtained for high resistivity silicon wafers. These results are most meaningful because the test masses of GW detectors will be made of high resistivity silicon with a minimum amount of impurities to reduce mechanical and optical losses. For the low resistivity silicon wafer, the calculated loss was much less than the measurement uncertainty. We used the low resistivity silicon wafer for the model verification and determined the measurement uncertainty.

The use of finite element analysis and the measured values of the electric field induced mechanical losses in disk resonators made of high-purity silicon allows one to calculate the associated electrostatic actuator thermal noise of GW detector test masses made of the same silicon.²⁸ By changing the configuration of the electrodes that create the electric field, it is possible to test different electrode patterns of the actuator in terms of achieving minimum induced losses and thermal noise. We can also check various operating regimes of the actuator by applying either a DC or an AC bias voltage to the electrodes. The developed experimental setup will also make it possible to measure these losses in silicon wafers with optical coatings. In the future, it is planned to cool down the silicon disk resonators and to study the electric field induced loss at 123 K. At this temperature, the coefficient of thermal expansion of silicon passes through zero, and therefore, the thermoelastic loss and associated noise are close to zero.8

ACKNOWLEDGMENTS

The authors are grateful to Ashot Markosyan for help with the measurement of the resistivity of silicon wafers and Edgard Bonilla for the valuable comments. This research was supported by the Interdisciplinary Scientific and Educational School of Moscow University "Fundamental and Applied Space Research" and funded by Russian Foundation for Basic Research under Project No. 19-29-11003. This paper was assigned LIGO Document No. LIGO-P2100057.

AUTHOR DECLARATIONS

Conflict of Interest

The authors declare that they have no conflicts of interest.

DATA AVAILABILITY

The data that support the findings of this study are available from the corresponding author upon reasonable request.

APPENDIX: SOLVING THE SYSTEM OF EQ. (2)

Consider the following system of differential equations:

$$\dot{q} = \frac{U_0}{R} - q \frac{1 + \beta x/d_0}{RC_1},\tag{A1}$$

$$m\ddot{x} + kx = -\frac{\beta^2 q^2 [1 - 2(1 - \beta)x/d_0]}{2C_0 d_0}.$$
 (A2)

When solving this system, we use the condition $x/d_0 \ll 1$. The electric field induced shift of the oscillator's resonant frequency and loss are small. So, we are looking for a solution in the form $x(t) = a\cos\omega t$ ($a\ll d_0$) and substitute it into Eq. (A1). We also assume that $\dot{x}\approx -a\omega\sin\omega t$. So, the equation for the charge q is a first order linear differential nonhomogeneous equation. First, we find the general solution of the corresponding homogeneous equation. Then, we solve the nonhomogeneous equation using the method variation of parameters. When expanding the exponential function in a series and performing the calculation, we keep only first order terms in a/d_0 . Finally, we obtain the following expression for the total charge q:

$$q(t) \approx \frac{U_0}{R} \left(RC_1 - \frac{a\beta}{\omega d_0} \frac{\omega RC_1}{1 + (\omega RC_1)^2} (\cos \omega t + \omega RC_1 \sin \omega t) \right). \tag{A3}$$

Substituting this q into the right side of Eq. (A2) and keeping only first order terms in a/d_0 , we obtain the following expression for the force acting on the oscillator:

$$F \approx -\frac{\beta^{2} U_{0}^{2}}{2C_{0} d_{0} R^{2}} \times \left[(RC_{1})^{2} - 2\frac{a}{d_{0}} \left(\frac{\beta}{\omega_{0}} \frac{\omega (RC_{1})^{2}}{1 + (\omega RC_{1})^{2}} \right) \right] \times \left(\cos \omega_{0} t + \omega RC_{1} \sin \omega_{0} t \right) - \left(RC_{1} \right)^{2} (1 - \beta) \cos \omega_{0} t \right]. \tag{A4}$$

There is a constant term in Eq. (A4) that is responsible for the static displacement of the oscillator mass. The term proportional to the displacement $x(t) = a \cos \omega t$ adds a stiffness to the oscillator,

$$\Delta k \approx -\frac{\beta^2 U^2}{C_0 d_0^2} \left[\frac{\beta C_1^2}{1 + (\omega R C_1)^2} + (1 - \beta) C_1^2 \right]. \tag{A5}$$

Since the relative change in the stiffness is small ($\Delta k/k \ll 1$), the relative change in the natural frequency of the oscillator is approximately equal to

$$\frac{\Delta\omega}{\omega_0} \approx \frac{1}{2} \frac{\Delta k}{m\omega_0^2}.\tag{A6}$$

Substituting Eq. (A5) into Eq. (A6), we obtain the final expression for the electric field induced frequency shift of the oscillator as follows:

$$\left(\frac{\Delta\omega}{\omega_0}\right)_E \approx -\frac{1}{2} \left(\frac{U_0}{d_0}\right)^2 \frac{C_0}{m\omega_0^2} \left[\frac{C_0}{C_1} \frac{1}{1 + (\omega_0 R C_1)^2} + \left(1 - \frac{C_0}{C_1}\right)\right]. \quad (A7)$$

The term in Eq. (A4) proportional to the velocity $\dot{x}(t) = -a\omega$ sin ωt adds loss Q_E^{-1} into the oscillator, which can be written as

$$Q_E^{-1} \approx \left(\frac{U_0}{d_0}\right)^2 \frac{C_0^2}{m\omega^2 C_1} \frac{\omega R C_1}{1 + (\omega R C_1)^2}.$$
 (A8)

REFERENCES

¹B. P. Abbott *et al.* (LIGO Scientific Collaboration and Virgo Collaboration), "Observation of gravitational waves from a binary black hole merger," Phys. Rev. Lett. **116**, 061102 (2016).

- ²J. Aasi *et al.*, "Characterization of the LIGO detectors during their sixth science run," Classical Quantum Gravity **32**, 115012 (2015).
- ³F. Acernese *et al.*, "Advanced Virgo: A second-generation interferometric gravitational wave detector," Classical Quantum Gravity **32**, 024001 (2014).
- ⁴R. Abbott *et al.* (LIGO Scientific Collaboration and Virgo Collaboration), "GWTC-2: Compact binary coalescences observed by LIGO and Virgo during the first half of the third observing run," Phys. Rev. X **11**, 021053 (2021).
- ⁵T. Akutsu *et al.*, "KAGRA: 2.5 generation interferometric gravitational wave detector," Nat. Astron. 3, 35–40 (2019).
- ⁶M. Punturo *et al.*, "The Einstein Telescope: A third-generation gravitational wave observatory," Classical Quantum Gravity **27**, 194002 (2010).
- ⁷E. D. Hall *et al.*, "Gravitational-wave physics with Cosmic Explorer: Limits to low-frequency sensitivity," Phys. Rev. D **103**, 122004 (2021).
- ⁸R. X. Adhikari *et al.*, "A cryogenic silicon interferometer for gravitational-wave detection," Classical Quantum Gravity **37**, 165003 (2020).
- ⁹S. M. Aston *et al.*, "Update on quadruple suspension design for Advanced LIGO," Classical Quantum Gravity **29**, 235004 (2012).
- ¹⁰E. Bonilla et al., "Method for electromechanical modeling of Johnson noise in Advanced LIGO," Classical Quantum Gravity 38, 025014 (2020).
- ¹¹G. Jourdan *et al.*, "Tuning the effective coupling of an AFM lever to a thermal bath," Nanotechnology **18**, 475502 (2007).
- ¹²T. Barois et al., "Ohmic electromechanical dissipation in nanomechanical cantilevers," Phys. Rev. B 85, 075407 (2012).
- ¹³N. E. Bousse *et al.*, "Quality factor tuning of micromechanical resonators via electrical dissipation," Appl. Phys. Lett. **116**, 023506 (2020).
- ¹⁴C. C. Speake *et al.*, "Electrostatic damping and its effect on precision mechanical experiments," Phys. Lett. A 263, 219–225 (1999).
- ¹⁵K. Yamamoto *et al.*, "Measurement of the mechanical loss of a cooled reflective coating for gravitational wave detection," Phys. Rev. D **74**, 022002 (2006).
- ¹⁶E. Hirose et al., "Mechanical loss of a multilayer tantala/silica coating on a sapphire disk at cryogenic temperatures: Toward the KAGRA gravitational wave detector," Phys. Rev. D 90, 102004 (2014).
- ¹⁷M. Abernathy et al., "Bulk and shear mechanical loss of titania-doped tantala," Phys. Lett. A 382, 2282–2288 (2018).
- ¹⁸G. Cagnoli *et al.*, "Mode-dependent mechanical losses in disc resonators," Phys. Lett. A **382**, 2165 (2018).
- ¹⁹E. Hirose et al., "Characterization of core optics in gravitational-wave detectors: Case study of KAGRA sapphire mirrors," Phys. Rev. Appl. 14, 014021 (2020).
- ²⁰G. Vajente *et al.*, "Method for the experimental measurement of bulk and shear loss angles in amorphous thin films," Phys. Rev. D **101**, 042004 (2020).
- ²¹K. Numata *et al.*, "Measurement of the intrinsic mechanical loss of low-loss samples using a nodal support," Phys. Lett. A **276**, 37–46 (2000).
- ²²E. Cesarini *et al.*, "A 'gentle' nodal suspension for measurements of the acoustic attenuation in materials," Rev. Sci. Instrum. **80**, 053904 (2009).
- ²³G. Vajente *et al.*, "A high throughput instrument to measure mechanical losses in thin film coatings," Rev. Sci. Instrum. **88**, 073901 (2017).
- ²⁴ A. Erwin *et al.*, "Electrostatic frequency reduction: A negative stiffness mechanism for measuring dissipation in a mechanical oscillator at low frequency," Rev. Sci. Instrum. **92**, 015101 (2021).
- ²⁵D. V. Martynov *et al.*, "Sensitivity of the Advanced LIGO detectors at the beginning of gravitational wave astronomy," Phys. Rev. D **93**, 112004 (2016).
- ²⁶V. Szekely, "On the representation of infinite-length distributed RC one-ports," IEEE Trans. Circuits Syst. **38**, 711–719 (1991).
- ²⁷L. G. Prokhorov *et al.*, "Measurement of mechanical losses in the carbon nanotube black coating of silicon wafers," Classical Quantum Gravity **37**, 015004
- ²⁸Y. Levin, "Internal thermal noise in the LIGO test masses: A direct approach," Phys. Rev. D 57, 659–663 (1998).